Supporting Information

Alkene Epoxidations with H_2O_2 over Groups 4-6 Metal-Substituted BEA Zeolites: Reactive Intermediates, Reaction Pathways, and Linear Free Energy Relationships

E. Zeynep Ayla, David S. Potts, Daniel T. Bregante, and David W. Flaherty*

Department of Chemical and Biomolecular Engineering
University of Illinois Urbana-Champaign, Urbana, IL 61801

*Corresponding Author
Phone: (217) 244-2816
Email: dwflhrty@illinois.edu

S1.0 *Ex situ* Characterization of M-BEA

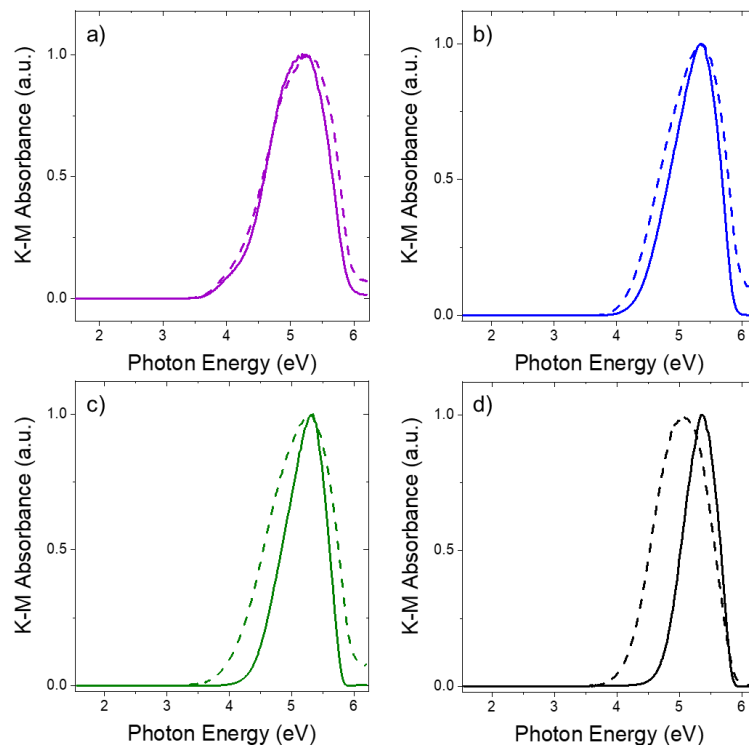## S1.1 Diffuse Reflectance UV-Vis Spectra of M-BEA

Figure S1. Tauc plots for M-BEA. Solid lines represent a low metal loading and dashed lines represent higher metal loading for (a) Mo-BEA, (b) Ti-BEA, (c) W-BEA, and (d) Nb-BEA.

The band gaps for M-BEA in these Tauc plots are much greater than those for their respective bulk metal oxides, implying the metals are dispersed when incorporated into the zeolite BEA framework. Calculated band gaps are summarized in **Table S1**.

Table S1. Metal loading and band gap for low and high metal loading M-BEA and band gap for corresponding metal oxide

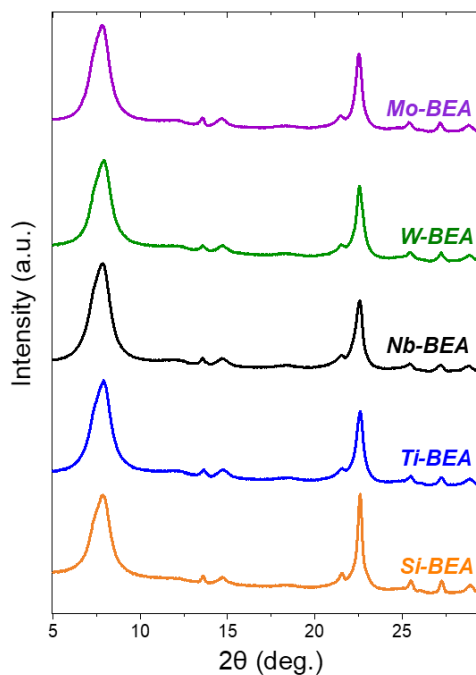| Catalyst	Low metal loading (solid lines)		High metal loading (dashed lines)		Bulk metal oxide band gap (eV)
	Metal loading (%)	Band gap (eV)	Metal loading (%)	Band gap (eV)	
Mo-BEA	0.40	3.96	3.2	3.92	2.9
Ti-BEA	0.25	4.34	1.8	4.07	3.2
W-BEA	0.55	4.41	7.8	3.85	2.8
Nb-BEA	0.22	4.73	3.5	4.1	3.4

S1.2 X-ray Diffraction of M-BEA

Figure S2. Powder X-ray diffractograms for 0.25 wt% Ti-BEA, 0.22 wt% Nb-BEA, 1.1 wt% W-BEA, and 0.4 wt % Mo-BEA under ambient conditions show the zeolite BEA structure is maintained after post-synthetic modification.

The similarities between the diffraction patterns of Si-BEA and metal-incorporated BEA suggest the structure of the BEA framework remains intact following dealumination and transition metal incorporation. At these low metal loadings (< 0.25 metal atoms per unit cell), the XRD features do not display observable shifts in the peak located at 22.5°. In our past work, we reported shifts towards greater diffraction angles when group 4 and 5 metals were incorporated into the BEA framework.[1] These shifts indicated an expansion of the zeolite lattice to accommodate these framework substituents.[1, 2] However, because these M-BEA have low metal density, the shift is less apparent in their diffractograms.
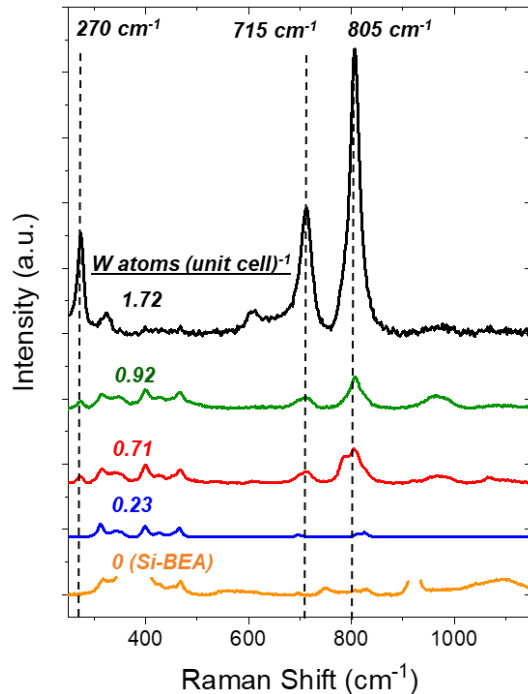
S1.3 Raman Spectra of Si-BEA and W-BEA

Figure S3. Raman spectra (442 nm, 0.8 mW μm^{-2}) of W-BEA pellets ($\sim$5-10 mg, 0.23 ( ), 0.71 (—), 0.93 (—), and 1.72 (—) W atoms per unit cell) under ambient conditions (Si-BEA (—) under 0.01 M H_2O_2 in CH_3CN flow 1 ml/min, 313 K). All spectra are rescaled to give a constant intensity for the 312 cm^{-1} feature of the BEA framework.

Ex situ Raman spectra of W-BEA show increasing intensities for the three vibrational modes indicative of bulk WO_3, which include 270 cm^{-1}, 715 cm^{-1}, and 805 cm^{-1}.[3] These trends show the emergence of extra-framework W atoms when loadings surpass 1 wt% (i.e., 0.23 W atoms per unit cell) that increase further with greater W loadings. Features between 300-550 cm^{-1} correspond to vibrations of the BEA framework.[4]

S2.0 *In situ* Characterization for H_2O_2 Activation on M-BEA

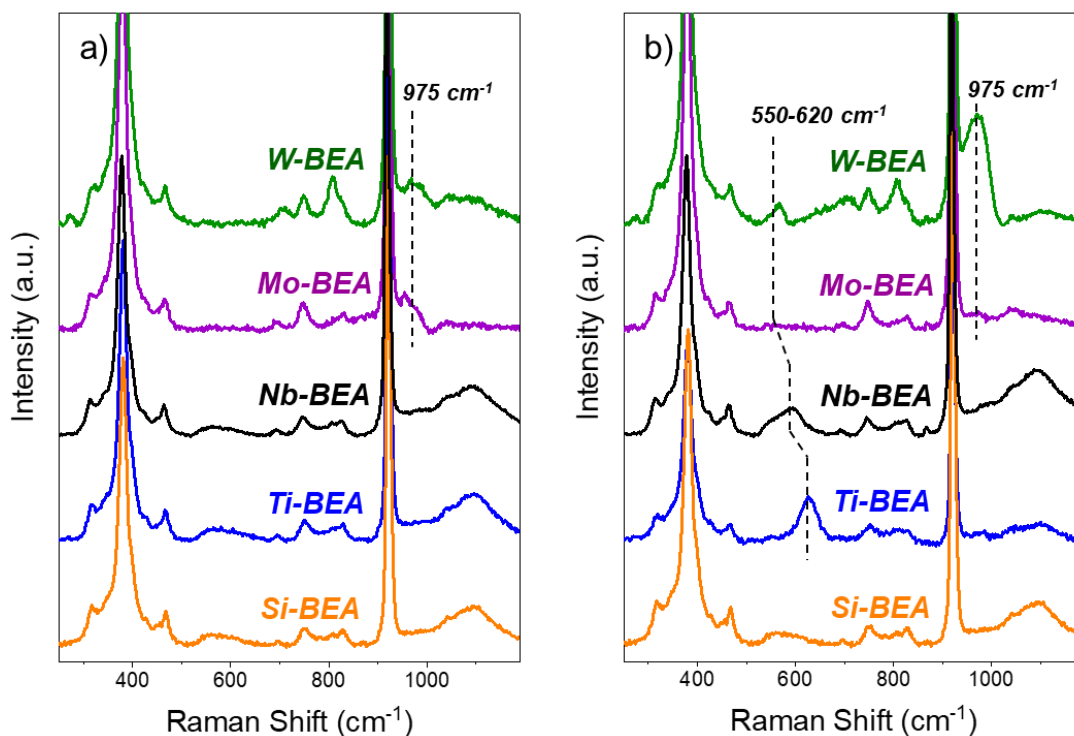### S2.1 *In Situ* Raman Spectra of M-BEA

Figure S4. Raman spectra (442 nm laser, 0.8 mW μm^{-2}) of M-BEA samples obtained (a) during contact with neat CH_3CN for 0.5 h, and (b) after 0.5 h contact with a flowing solution of H_2O_2 in CH_3CN (10 mM H_2O_2, 39 mM H_2O in CH_3CN; 1 ml min^{-1}) at 313 K. Spectra of Si-, Ti-, Nb-, and W-BEA are taken at steady-state, whereas Mo-BEA shows further changes following 20 min. All spectra are normalized to the BEA framework feature at 312 cm^{-1}. M-BEA synthesized with high metal content (1.2 wt % Ti, 3 wt % Nb, 5 wt % W, 5 wt % Mo) are used to increase Raman peak intensity and clearly observe features unique to H_2O_2 activation on incorporated metal atoms.

Figure S4a shows features on M-BEA in flowing neat CH_3CN (1 ml min^{-1}) prior to contact with H_2O_2, and these spectra contain features indicative of oxygen ligands (e.g., metal-oxos; M=O) on Mo-BEA and W-BEA at 950-975 cm^{-1}.[3, 5] Features between 694-825 cm^{-1} are framework vibrations of Si-BEA[4] and appear in all spectra. Subsequently, the liquid stream is changed to a H_2O_2 solution (10 mM H_2O_2, 39 mM H_2O in CH_3CN; 1 ml min^{-1}), and Figure S4b shows spectra obtained after 0.5 h. These spectra include a new vibrational feature between 550-620 cm^{-1} on Ti-BEA, Nb-BEA, and W-BEA, which corresponds to a Raman-enhanced vibration mode that represents the formation of metal-peroxo (M-η^2-O_2) species.[3, 6, 7] Metal-peroxo species exist in equilibrium with metal-hydroperoxo species (M-OOH),[8, 9] which can be detected by UV-Vis (Section S2.2.) but have yet to be reliably detected by Raman spectroscopy.[6] In contrast, Raman spectra of Mo-BEA in flowing H_2O_2 solutions exhibit a short-lived peak around 560 cm^{-1} (not shown here but in Figure 2), which indicates the initial formation of a Mo-η^2-O_2 intermediate. However, all features corresponding to Mo atoms within the BEA framework disappear after 0.5 h contact with flowing H_2O_2. These changes show the loss of Mo atoms from the zeolite framework, which agrees with results from energy-dispersive X-ray fluorescence (EDXRF) that show the loss of at least 90 % of Mo atoms from the sample after the experiment concludes.

Note: Figure S4a contains a feature around 560 cm^{-1} on Si-, Ti-, and Nb-BEA samples that may indicate a relatively lower degree of crystallinity of the BEA framework.[10] We believe the absence of this feature on W- and Mo-BEA, which are synthesized using the same parent batch of dealuminated BEA, may result from a slight change in the focus of the laser or shift in the position of the pellet during the experiment.
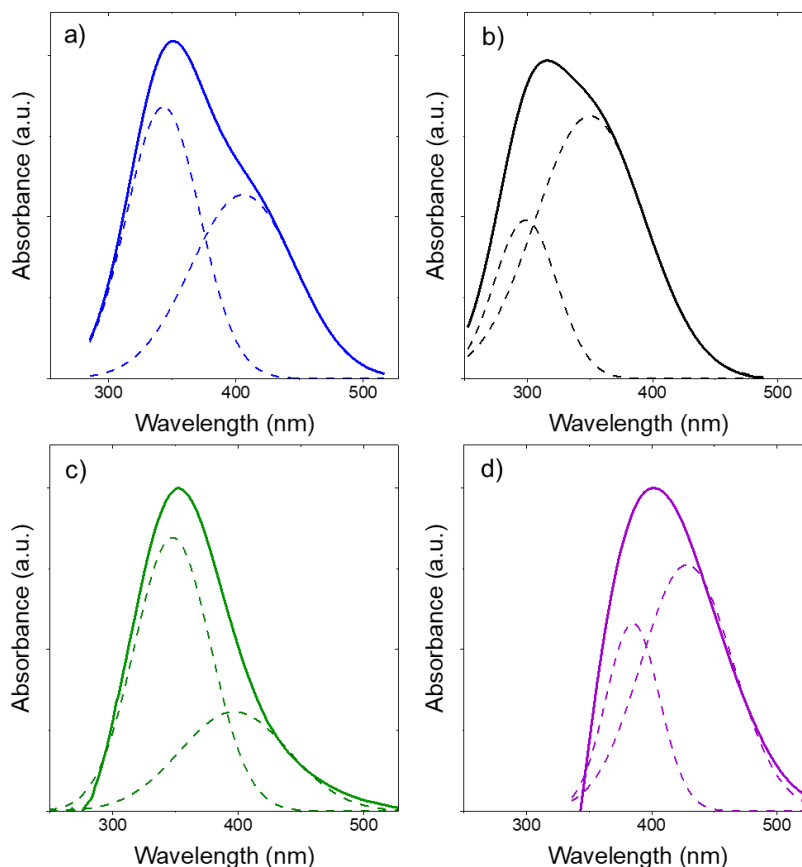
S2.2 *In situ* UV-Vis Spectra of M-BEA

Figure S5. *In situ* UV-Vis spectra for (a) Ti-BEA (0.25 wt %), (b) Nb-BEA (0.22 wt %), (c) W-BEA (1.1 wt %), and (d) Mo-BEA (0.40 wt %) while flowing a solution of H_2O_2 (10 mM H_2O_2, 39 mM H_2O, in CH_3CN, 1 ml min^{-1}) at 313 K. Each spectrum shows the difference between the H_2O_2-activated sample and the corresponding UV-Vis spectrum for the bare M-BEA sample, and all difference spectra are normalized to the maximum absorbance value.

Figure S5 shows steady-state UV-Vis spectra of reactive intermediates formed upon M-BEA samples by activation of solution-phase H_2O_2 (10 mM H_2O_2, 39 mM H_2, in CH_3CN, 1 ml min^{-1}) at 313 K. These spectra are deconvoluted by subtracting a baseline and fitting Gaussian functions to two features (fixed baseline at 0, initial guesses for peak positions are determined by literature values for LMCT bands of M-(η^2-O_2) and M-OOH) using OriginPro software. The two resulting features represent the individual contributions of M-(η^2-O_2) and M-OOH surface intermediates formed at framework transition metal atoms and to give the ligand-to-metal charge transfer (LMCT) energies for these oxygen ligands. M-(η^2-O_2) species absorb photons at higher energies (shorter λ) than M-OOH species.[6, 11-14] The relative LMCT energies of active oxygen species correlates with the electrophilicity of the reactive intermediates, which can be related to turnover rates and apparent activation enthalpies for alkene epoxidation[15] and thiophene oxidations[16] on group 4 and 5 transition metal substituted BEA catalysts.

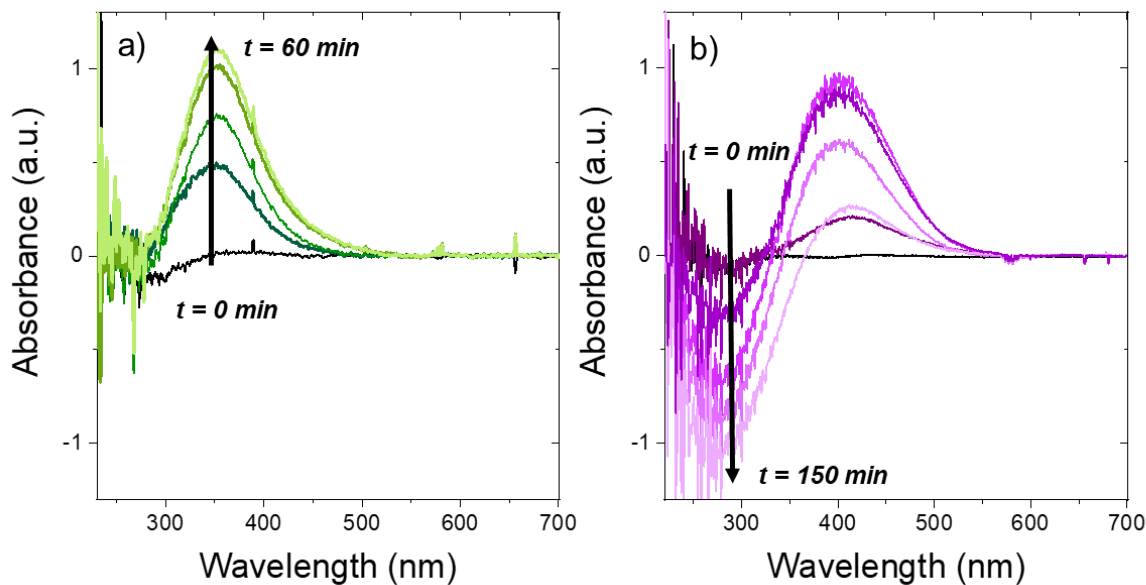## S2.3 Transient *In Situ* UV-Vis Spectra of W-BEA and Mo-BEA

Figure S6. *In situ* UV-Vis spectra of (a) W-BEA (1.1 wt %), and (b) Mo-BEA (0.4 wt %) pellets within flowing solutions of H_2O_2 (10 mM H_2O_2, 39 mM H_2O, in CH_3CN, 1 cm^3 min^{-1}) at 313 K. Each spectrum shows the difference between the M-BEA sample after contact with H_2O_2 for a given period of time and the corresponding UV-Vis spectrum for the M-BEA sample in a solution of CH_3CN (39 mM H_2O in CH_3CN, 1 cm^3 min^{-1}) at 313K, and all difference spectra are normalized such that the maximum absorbance for the LMCT band in the series corresponds to a value of unity.

Figure S6 shows time-resolved *in situ* UV-Vis spectra for W-BEA and Mo-BEA within flowing H_2O_2 solutions (10 mM H_2O_2, 39 mM H_2, in CH_3CN, 1 ml min^{-1}) at 313 K. These series of spectra show the formation of M-η^2-O_2 and M-OOH intermediates with LMCT features for M-(η^2-O_2) at 310 nm (W-BEA) and 360 nm (Mo-BEA)[12] and for M-OOH at lower energies, as an extension of assignments for Ti-BEA and Nb-BEA.[11, 13, 17] The UV-Vis features for H_2O_2-activated W-BEA attain steady-state after 1 h, however, the intensity of the absorbance features for Mo-BEA increase initially but then decrease with time. The features at lower wavelengths (< 300 nm) represent charge transfer from Mo centers to the zeolite framework. These features become increasingly negative during the course of the experiment, which indicates the dissolution and loss of Mo atoms from the BEA framework[18] consistent with the discussion of Raman spectra and EDXRF results in Section S2.1.

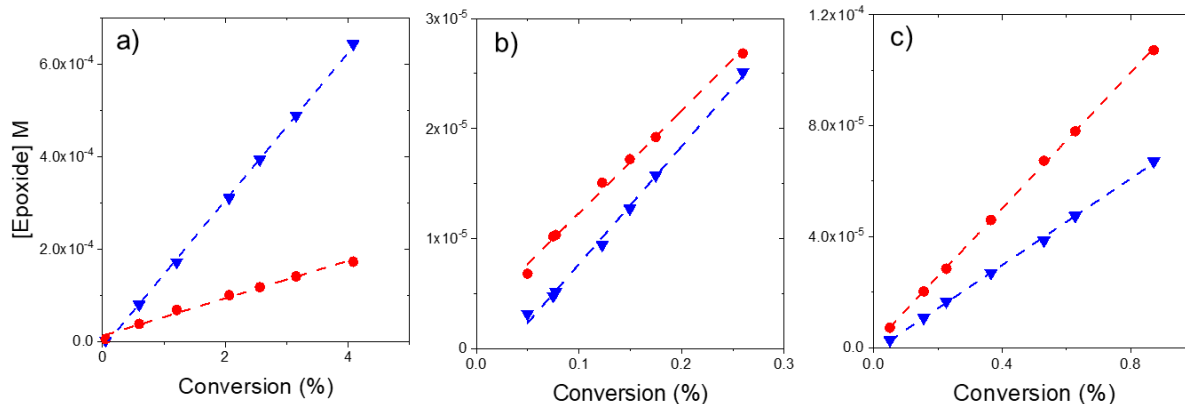## S3.0 Product Distributions for Cis-Stilbene Epoxidation with H_2O_2 over M-BEA

Figure S7. Concentrations of trans-stilbene epoxide (●) and cis-stilbene epoxide (▼) formed during the epoxidation of cis-stilbene (20 mM) with H_2O_2 as functions of cis-stilbene conversion over (a) Ti-BEA (0.25 wt %), (b) Nb-BEA (0.22 wt %), (c) W-BEA (1.1 wt %) in CH_3CN solutions (10 mM H_2O_2, 39 mM H_2O) at 313 K.

Figure S7 shows the concentrations of cis- and trans-stilbene epoxide formed by the epoxidation of cis-stilbene as functions of cis-stilbene conversion over Ti-, Nb-, and W-BEA samples in acetonitrile (20 mM cis-stilbene, 10 mM H_2O_2, 39 mM H_2O, in CH_3CN) at 313 K. These concentration profiles indicate that both epoxide isomers are primary products and the difference between their relative concentrations among the M-BEA catalysts suggest that distinct reactive intermediates epoxidize alkenes on each material. Trans-stilbene epoxide forms through a multi-step homolytic mechanism for oxygen transfer from M-(η^2-O_2) intermediates to alkenes, which allows rotation of the C-C bond and gives nearly equimolar mixtures of trans- and cis-stilbene epoxides. In contrast, M-OOH and M=O species primarily produce cis-stilbene epoxide as a consequence of a concerted mechanism that does not permit isomerization during oxygen atom transfer to the C=C bond.[19, 20] Product distributions over M-BEA suggest Ti-BEA reacts primarily through Ti-OOH, because cis-stilbene epoxide is the predominant product. More similar quantities of cis- and tran-stilbene epoxides form over Nb-BEA and W-BEA, which implies that these catalysts epoxidize alkenes primarily with M-(η^2-O_2) species.

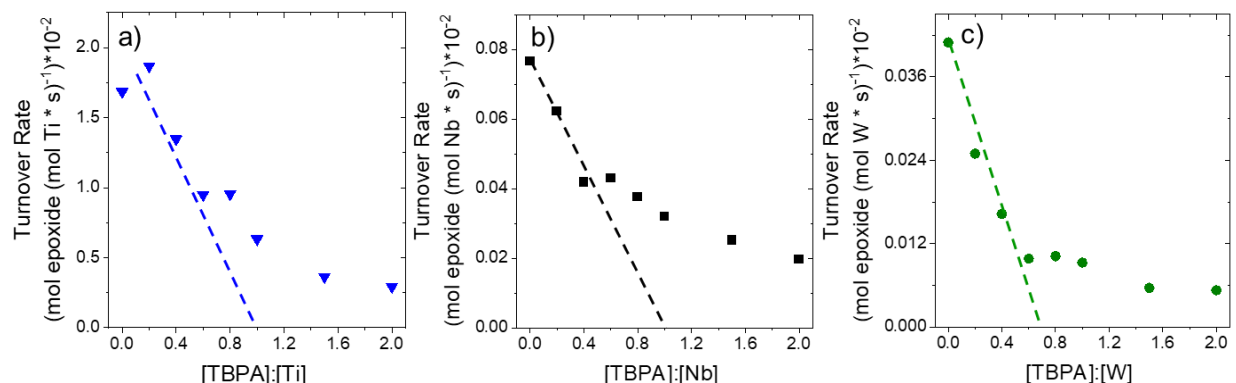## S4.0 *In Situ* Tert-Butyl Phosphonic Acid Site Titrations of M-BEA

Figure S8. Tert-butyl phosphonic acid titrations of (a) Ti-BEA (0.25 wt %), (b) Nb-BEA (0.22 wt %), (c) W-BEA (1.1 wt %) during 1-hexene epoxidation with H_2O_2 in CH_3CN (10 mM C_6H_{12}, 10 mM H_2O_2, 39 mM H_2O, in CH_3CN) at 313 K.

The number of catalytically active metal atoms within each M-BEA sample were determined by *in situ* tert-butyl phosphonic acid (TBPA) site titrations. TBPA was introduced to a solution of 1-hexene and acetonitrile in a round bottom flask that contained the suspended M-BEA catalyst. The mixture was stirred for 0.5 h with the intent to equilibrate the coverage of TBPA on framework metal atoms. Then, H_2O_2 was added to initiate the reaction. The rates shown in Figure S8 are normalized by total metal content determined by EDXRF. As the ratio of the concentration of TBPA to total metal atoms ([TPBA]:[M]) increases, the normalized rates for epoxidation decrease, because TBPA binds to a greater fraction of the metal sites. Extrapolation of the initial few linear points to the abscissa indicates that nearly 100 % of Ti and Nb atoms present form active sites for 1-hexene epoxidation, while ~70% of W atoms catalyze the epoxidation reaction. Inactivation of some incorporated W atoms is likely due to oligomerization (Figure S3 and Figure S9). Turnover rates, activation enthalpies, and enthalpies of 1,2-epoxyhexane adsorption reported in the main text were acquired from these specific M-BEA catalysts.
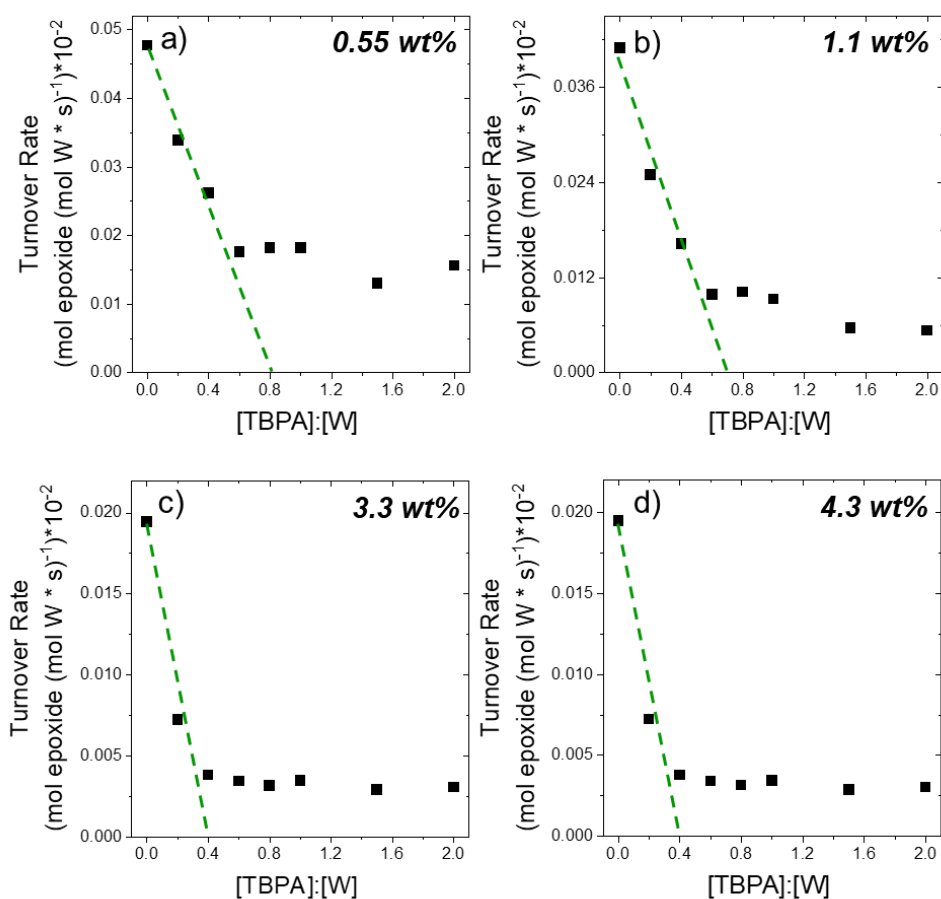
Figure S9. Tert-butyl phosphonic acid titrations of W-BEA with various W loadings (a) 0.55 wt %, (b) 1.1 wt %, (c) 3.3 wt %, and (d) 4.3 wt % during 1-hexene epoxidation with H_2O_2 in CH_3CN (10 mM C_6H_{12}, 1 mM H_2O_2, 39 mM H_2O, in CH_3CN) at 313 K.

Site titrations were performed as discussed in sections 2.2 and 4.1. As W loading (as measured by EDXRF) increases, percentage of sites active for 1-hexene epoxidation decreases. This is likely due to the tendency of W to oligomerize and form clusters of WO_3 as suggested by increasing band gap (Figure S1) and more intense Raman features for WO_3 (Figure S3) at higher W loadings. The percentage of active W atoms decreases with increasing W loading.

Table S2. Percentage of active W atoms and band gaps for W-BEA with increasing total W content

W content (wt %)[a]	Metal atoms per unit cell	Band gap (eV)[b]	Active metal (%)[c]
0.55	0.12	4.41	80
1.1	0.23	4.30	70
3.3	0.71	4.13	50
4.3	0.93	4.10	40

[a]measured by EDXRF (Section 2.2), [b]determined by DRUV-vis (Section 2.2, Figure S1), [c]determined by *in situ* tert-butyl phosphonic acid titrations (Section 2.3, Figure S8)

S5.0 Derivation of Rate Expression for 1-Hexene Epoxidation with H_2O_2 and H_2O_2 Decomposition over M-BEA
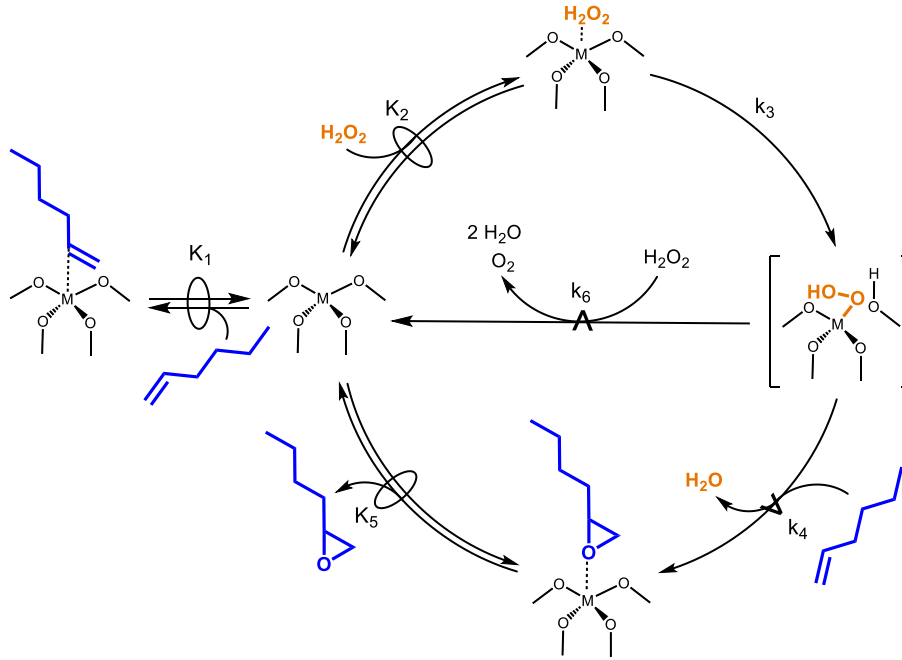
Scheme 2 (from main text). Proposed mechanism for 1-hexene epoxidation with H_2O_2 and H_2O_2 decomposition depicted for group 4 M-BEA. The ⊖ symbol denotes a quasi-equilibrated step and the ⋀ symbol signifies the kinetically relevant steps for the formation of distinct products.

Scheme 2 illustrates a series of elementary steps beginning with the quasi-equilibrated adsorption of 1-hexene (C_6H_{12}) (step 1) and hydrogen peroxide, H_2O_2 (step 2) which is followed by the irreversible activation of H_2O_2 to M-OOH (step 3) or M-(η^2-O_2). Activation of H_2O_2 can result in H_2O_2 decomposition (step 6) or kinetically relevant epoxidation (step 4) by reacting with a H_2O_2 molecule or C_6H_{12} molecule, respectively. The epoxide undergoes quasi-equilibrated adsorption to form 1,2-epoxyhexane [$C_6H_{12}O$] as the product. Measured rates result from the reaction of H_2O-derived surface species with a C_6H_{12} molecule represented by the following equation:

$$r_E = k_4[M - OOH][C_6H_{12}] \tag{S1}$$

Applying the pseudo-steady state hypothesis to M-OOH species, produces Equation S2:

$$r_E = \frac{k_3\, k_4\, K_2 [C_6H_{12}][H_2O_2][*]}{k_4[C_6H_{12}] + k_6[H_2O_2]} \tag{S2}$$

where r_E is the epoxidation rate, k_4 is the rate constant for step 4 in Scheme 2, and $[M - OOH]$ represents the number of H_2O_2-activated metal sites. The total number of sites, *[L]*, represents all occupied and unoccupied active sites:

$$[L] = [*] + [* \, C_6H_{12}] + [* \, H_2O_2] + [* \, OOH] + [* \, C_6H_{12}O] \tag{S3}$$

where $[*]$ is the number of unoccupied sites and $[* \, OOH]$, $[* \, C_6H_{12}]$, $[* \, H_2O_2]$, and $[* \, C_6H_{12}O]$ represent the number of activated H_2O_2, and adsorbed C_6H_{12}, H_2O_2, and $C_6H_{12}O$ respectively. Replacing each term with the associated rate and equilibrium constants, and reactant and product concentrations gives:

$$[L] = 1 + K_1[C_6H_{12}] + K_2[H_2O_2] + \frac{k_3 K_2\, [H_2O_2]}{k_4[C_6H_{12}] + k_6[H_2O_2]} + \frac{[C_6H_{12}O]}{K_5} \tag{S4}$$

Bringing together equations S2 and S4 yields the rate expression for $C_6H_{12}O$ formation (equation 2 in main text):

$$\frac{r_E}{[L]} = \frac{\dfrac{k_3 k_4 K_2 [H_2O_2][C_6H_{12}]}{k_4[C_6H_{12}] + k_6[H_2O_2]}}{1 + K_1[C_6H_{12}] + K_2[H_2O_2] + \dfrac{k_3 K_2 [H_2O_2]}{k_4[C_6H_{12}] + k_6[H_2O_2]} + \dfrac{[C_6H_{12}O]}{K_5}} \tag{S5}$$

Similarly, measured rates for H_2O_2 decomposition depend on the reaction between H_2O_2 and M-OOH or M-(η^2-O_2) to produce O_2 and H_2O.

$$r_D = k_6[M - OOH][H_2O_2] \tag{S6}$$

Using the same site balance, *[L]* as above, we define turnover rates for H_2O_2 decomposition as:

$$\frac{r_D}{[L]} = \frac{\dfrac{k_3 k_4 K_2 [H_2O_2]^2}{k_4[C_6H_{12}] + k_6[H_2O_2]}}{1 + K_1[C_6H_{12}] + K_2[H_2O_2] + \dfrac{k_3 K_2 [H_2O_2]}{k_4[C_6H_{12}] + k_6[H_2O_2]} + \dfrac{[C_6H_{12}O]}{K_5}} \tag{S7}$$

At low of $[C_6H_{12}]:[H_2O_2]$, the surface of M-BEA is saturated with species derived from H_2O_2 and rates of H_2O_2 decomposition increase as a linear function of $[H_2O_2]$.[15] The term that represents these species dominates, simplifying the rate expression to:

$$\frac{r_D}{[L]} = k_6[H_2O_2] \tag{S8}$$

S6.0 Heats per Injection of 1,2-Epoxyhexane and Thermograms for Isothermal Titration Calorimetry
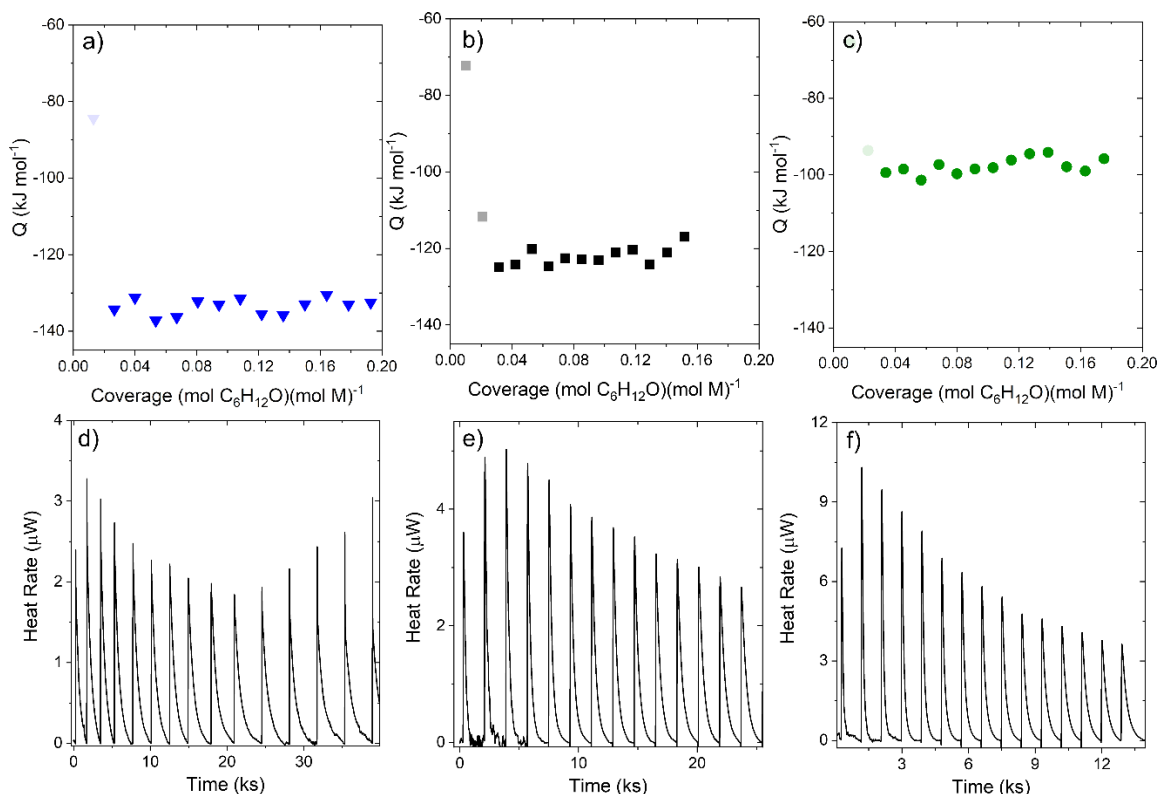

Figure S10. Heats released upon 1,2-epoxyhexane adsorption in CH_3CN (39 mM H_2O, 313 K) on (a) Ti-BEA (▼), (b) Nb-BEA (■), and (c) W-BEA (●) as a function of 1,2-epoxyhexane coverage and associated thermograms for (d) Ti-BEA, (e) Nb-BEA, and (f) W-BEA.

Adsorption enthalpies for 1,2-epoxyhexane ($\Delta H_{ads,epox}$) on M-BEA were measured by isothermal titration calorimetry. Values of $\Delta H_{ads,epox}$ were most negative for Ti-BEA suggesting Ti-BEA adsorbs the epoxide more strongly than Nb-BEA and W-BEA.

Note: The reason for the lower heat value for the initial injection of each thermogram above (Figure S10d-f) is due to the experimental set-up. For each experiment, before the titrant-filled syringe is loaded into the instrument, the tip of the syringe needle is blotted to remove small amount of excess liquid. This blotting, along with natural evaporation, removes a small amount of liquid at the tip of the needle. Moreover, during initial equilibration, diffusion occurs at the liquid at the tip of the needle due to the concentration gradient. This results in the first injection containing less titrant than intended and therefore, noticeable error in the first injection.

S7.0 Effects of Electronegativity on 1-Hexene Epoxidation Apparent Activation Enthalpies and 1,2-Epoxyhexane Adsorption Enthalpies
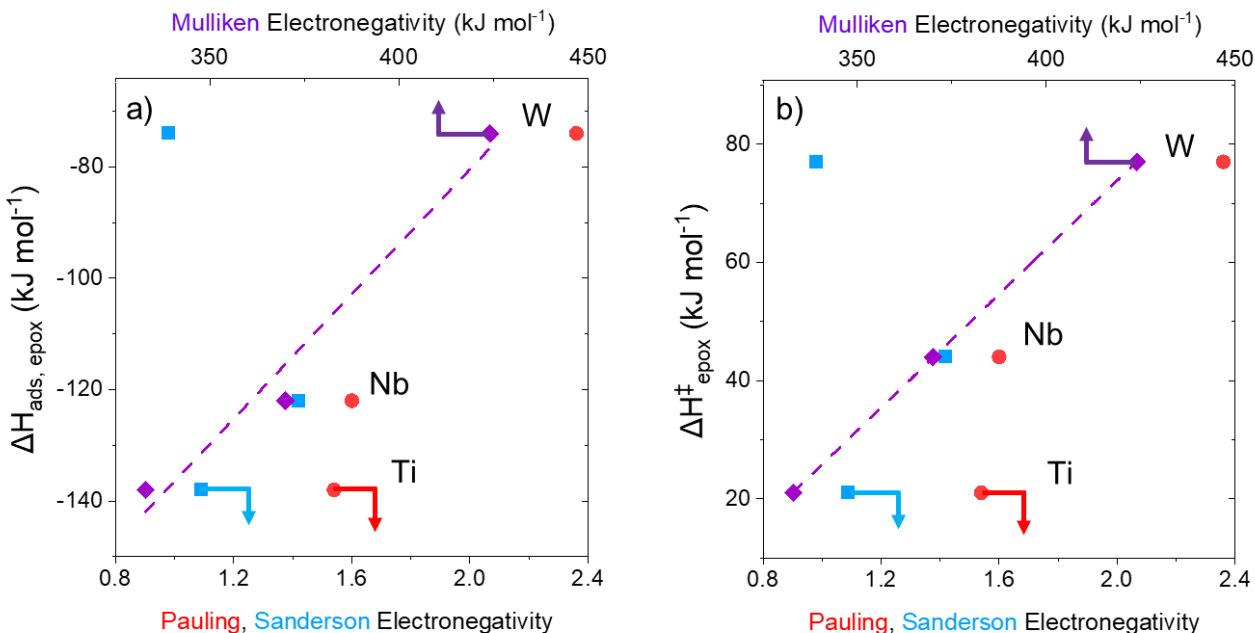

Figure S11. Measured (a) $C_6H_{12}O$ adsorption enthalpies $\Delta H_{ads,epox}$ and (b) apparent activation enthalpies $\Delta H^{\ddagger}_{epox}$ are plotted against Pauling[21] (●), Sanderson (■), and Mulliken electronegativities[22] (♦).

None of the electronegativity scales fit the initial hypothesis that more electronegative metals will lead to the synthesis of more electrophilic sites, and therefore lower activation barriers for epoxidation. However, a linear trend (opposite of our hypothesis) is observed for Mulliken electronegativity (average of electron affinity[23] and first ionization energy[24]) values as a function of 1-hexene epoxidation enthalpies and 1,2-epoxyhexane adsorption enthalpies on M-BEA. Nb and W are more electronegative than Ti on the Mulliken scale which may explain the greater number of pendant oxygen ligands that form on these metals when they are incorporated into the zeolite BEA framework. However, these ligands ultimately result in a more diffuse electron density, making these oxygen species, some of which are reactive intermediates, less electrophilic. This may explain the higher epoxidation activation enthalpies for the more electronegative Nb and W in BEA and why 1,2-epoxyhexane binds weaker to Nb and W active sites than those of Ti in BEA.

References

1.   Bregante, D. T.; Johnson, A. M.; Patel, A. Y.; Ayla, E. Z.; Cordon, M. J.; Bukowski, B. C.; Greeley, J.; Gounder, R.; Flaherty, D. W., Cooperative Effects between Hydrophilic Pores and Solvents: Catalytic Consequences of Hydrogen Bonding on Alkene Epoxidation in Zeolites. *Journal of the American Chemical Society* **2019,** *141* (18), 7302-7319.

2.   Baran, R.; Millot, Y.; Onfroy, T.; Krafft, J.-M.; Dzwigaj, S., Influence of the nitric acid treatment on Al removal, framework composition and acidity of BEA zeolite investigated by XRD, FTIR and NMR. *Microporous and Mesoporous Materials* **2012,** *163*, 122-130.

3.   Ross-Medgaarden, E. I.; Wachs, I. E., Structural Determination of Bulk and Surface Tungsten Oxides with UV–vis Diffuse Reflectance Spectroscopy and Raman Spectroscopy. *The Journal of Physical Chemistry C* **2007,** *111* (41), 15089-15099.

4.   Mihailova, B.; Valtchev, V.; Mintova, S.; Faust, A. C.; Petkov, N.; Bein, T., Interlayer stacking disorder in zeolite beta family: a Raman spectroscopic study. *Physical Chemistry Chemical Physics* **2005,** *7* (14), 2756.

5.   Hu, H.; Wachs, I. E.; Bare, S. R., Surface Structures of Supported Molybdenum Oxide Catalysts: Characterization by Raman and Mo L3-Edge XANES. *The Journal of Physical Chemistry* **1995,** *99* (27), 10897-10910.

6.   Bordiga, S.; Damin, A.; Bonino, F.; Ricchiardi, G.; Lamberti, C.; Zecchina, A., The Structure of the Peroxo Species in the TS-1 Catalyst as Investigated by Resonant Raman Spectroscopy. *Angewandte Chemie International Edition* **2002,** *41* (24), 4734-4737.

7.   Maniatakou, A.; Karaliota, S.; Mavri, M.; Raptopoulou, C.; Terzis, A.; Karaliota, A., Synthesis, characterization and crystal structure of novel mononuclear peroxotungsten(VI) complexes. Insulinomimetic activity of W(VI) and Nb(V) peroxo complexes. *Journal of Inorganic Biochemistry* **2009,** *103* (5), 859-868.

8.   Yoon, C. W.; Hirsekorn, K. F.; Neidig, M. L.; Yang, X.; Tilley, T. D., Mechanism of the Decomposition of Aqueous Hydrogen Peroxide over Heterogeneous TiSBA15 and TS-1 Selective Oxidation Catalysts: Insights from Spectroscopic and Density Functional Theory Studies. *ACS Catalysis* **2011,** *1* (12), 1665-1678.

9.   Bregante, D. T.; Thornburg, N. E.; Notestein, J. M.; Flaherty, D. W., Consequences of Confinement for Alkene Epoxidation with Hydrogen Peroxide on Highly Dispersed Group 4 and 5 Metal Oxide Catalysts. *ACS Catalysis* **2018,** *8* (4), 2995-3010.

10.   Tosheva, L.; Mihailova, B.; Valtchev, V.; Sterte, J., Zeolite beta spheres. *Microporous and Mesoporous Materials* **2001,** *48* (1-3), 31-37.

11.   A. Zecchinaa , S. B., G. Spotoa, A. Damina, G. Berliera, F. Boninoa, C. Prestipinoaand C. Lamberti, In situ characterization of catalysts active in partial oxidations: TS-1 and Fe-MFI case studies. *Topics in Catalysis* **2002,** *21*, 67-78.

12.   Maurya, M. R., Bharti, N., Synthesis, thermal and spectral studies of oxoperoxo and dioxo complexes of vanadium(V), molybdenum(VI) and tungsten(VI) with 2-(a-hydroxyalkyl/aryl)benzimidazole. *Transition Metal Chemistry* **1999,** (24), 389-393.

13.   Shetti, V. N.; Manikandan, P.; Srinivas, D.; Ratnasamy, P., Reactive oxygen species in epoxidation reactions over titanosilicate molecular sieves. *Journal of Catalysis* **2003,** *216* (1-2), 461-467.

14.   Ziolek, M.; Sobczak, I.; Decyk, P.; Wolski, L., The ability of Nb2O5 and Ta2O5 to generate active oxygen in contact with hydrogen peroxide. *Catalysis Communications* **2013,** *37*, 85-91.

15.   Bregante, D. T.; Flaherty, D. W., Periodic Trends in Olefin Epoxidation over Group IV and V Framework-Substituted Zeolite Catalysts: A Kinetic and Spectroscopic Study. *Journal of the American Chemical Society* **2017,** *139* (20), 6888-6898.

16.   Bregante, D. T.; Patel, A. Y.; Johnson, A. M.; Flaherty, D. W., Catalytic thiophene oxidation by groups 4 and 5 framework-substituted zeolites with hydrogen peroxide: Mechanistic and spectroscopic evidence for the effects of metal Lewis acidity and solvent Lewis basicity. *Journal of Catalysis* **2018,** *364*, 415-425.

17.   Ziolek, M.; Sobczak, I.; Decyk, P.; Sobańska, K.; Pietrzyk, P.; Sojka, Z., Search for reactive intermediates in catalytic oxidation with hydrogen peroxide over amorphous niobium(V) and tantalum(V) oxides. *Applied Catalysis B: Environmental* **2015,** *164*, 288-296.

18.   Williams, C. C.; Ekerdt, J. G.; Jehng, J. M.; Hardcastle, F. D.; Turek, A. M.; Wachs, I. E., A Raman and ultraviolet diffuse reflectance spectroscopic investigation of silica-supported molybdenum oxide. *The Journal of Physical Chemistry* **1991,** *95* (22), 8781-8791.

19.   Cundari, T. R.; Drago, R. S., Molecular orbital investigation of ruthenium-oxo-catalyzed epoxidations. *Inorganic Chemistry* **1990,** *29* (3), 487-493.

20.   Dobson, J. C.; Seok, W. K.; Meyer, T. J., Epoxidation and catalytic oxidation of olefins based on a RuIV:O/RuII-OH2 couple. *Inorganic Chemistry* **1986,** *25* (10), 1513-1514.

21.   Oxtoby, D. W. G., H.P.; Campion, A. , *Principles of Modern Chemistry*. 7th ed.; Cengage Learning: 2012.

22.   Mulliken, R. S., A New Electroaffinity Scale; Together with Data on Valence States and on Valence Ionization Potentials and Electron Affinities. *Journal of Chemical Physics* **1934,** *2*.

23.   Myers, R. T., The Periodicity of Electron Affinity. *Journal of Chemical Education* **1990,** *67*, 307-308.

24.   Brown, T. L. L., Jr., H. E.; Bursten; B. E.; Murphy, C. J.; Woodward, P. M. , *Chemistry: The Central Science*. 12th ed.; Pearson: 2012.